RSC Advances

PAPER

View Article Online
View Journal | View Issue

Cite this: *RSC Adv.*, 2020, **10**, 38524

Micron-sized SiO_x/N-doped carbon composite spheres fabricated with biomass chitosan for high-performance lithium-ion battery anodes†

Dajin Liu,[ab] Zhipeng Jiang,[ab] Wei Zhang,[a] Jingqi Ma[ab] and Jia Xie *[a]

To achieve superior lithium storage performance, SiO_x is usually designed into nanostructured SiO_x/C composites by complex or expensive methods. Here, micron-sized interconnected SiO_x/N-doped carbon (NC) microspheres composed of evenly dispersed SiO_x nano-domains and NC have been fabricated by a scalable microemulsion method and following pyrolysis, using vinyltriethoxysilane and chitosan as precursors. The unique structure of the micron-sized SiO_x/NC spheres leads to enhanced structural integrity and enables stable long-term cycling (800 cycles at 2 A g^{-1}). Benefiting from the enhanced electron/Li^+ diffusion kinetics originated from the unique structure and N-doping, SiO_x/NC-2 presents considerable capacitive-controlled Li storage capacity, which leads to outstanding rate capability. Consequently, the assembled SiO_x/NC-2//$LiFePO_4$ full cell exhibits superior rate capability (106 mA h g^{-1} at 4C) and stable long-term cycling at 2C (102 mA h g^{-1} after 350 cycles). This work opens a new door for the application of chitosan in building micron-sized high-performance SiO_x/C anode materials, and to some extent facilitates the recycling of waste seafood shells.

Received 15th August 2020
Accepted 10th October 2020

DOI: 10.1039/d0ra07029g

rsc.li/rsc-advances

Introduction

With high energy density and long cycle life, rechargeable Li-ion batteries (LIBs) have been widely used as a power source for smartphones and electronic vehicles (EVs), and greatly fueled their development in the past two decades.[1–5] However, traditional LIBs with graphite as anodes cannot satisfy the rapidly growing need for high energy density. Aiming at improving the energy and power density of LIBs, a series of high-capacity new anode materials have been explored. Among them, Si-based materials are considered as the most promising ones for industrial application, because of their super-high theoretical capacity, appropriate working voltage and natural abundance.[6–8] Unfortunately, the Si anode suffers from huge volume change during cycling and poor conductivity, both of which lead to poor cycling stability.[9,10] Benefiting from the reduced volume variation during cycling and the buffering effect of *in situ* generated lithium silicates and Li_2O,[11,12] SiO_x anodes generally maintain better cycling stability than the Si anodes.[12–14] However, SiO_x also needs to be combined with other conductive buffer materials at the nano-scale because of its poor electron/Li^+ conductivity and non-negligible volume change during charge/discharge processes.

It has been reported that carbon can effectively improve the conductivity and structural integrity of SiO_x.[15–17] In order to enhance cycling stability, coulombic efficiency, and rate capability, SiO_x is usually designed as nanostructured SiO_x/C composites.[15–32] Stöber method is one of the most commonly used methods for constructing SiO_x/C nanocomposites. But the extensive requirement of solvents lowers its availability. Moreover, to substantially enhance conductivity and mechanical property, graphene (oxides) and carbon nanotubes are massively used in some SiO_x/C composite materials, which inevitably increases the cost of the prepared SiO_x/C composites and hinders their mass production.[20,31,33,34] Thus it is desirable to prepare SiO_x/C anode materials by using more available methods, low-cost and renewable carbon precursors, and achieve superior lithium storage performance.

Chitosan (CS), extracted from waste crab and shrimp shells, is one of the most abundant and least expensive natural polymers on earth.[35,36] Every year, 6–8 million tons of such waste shells are generated from the seafood industry globally, and many of them are directly dumped in landfills or the sea.[37] The industrial application of chitin and CS can not only realize the recycling of waste, but also ease the pressure on the environment.[38,39] Recently, CS has been used to develop CS-based binders and gel polymer electrolytes for LIBs and Li-ion capacitors (LICs).[40–45] Because of its high nitrogen content, CS is also a favored precursor for electrode materials such as N-

[a]State Key Laboratory of Advanced Electromagnetic Engineering and Technology, School of Electrical and Electronic Engineering, Huazhong University of Science and Technology, Wuhan 430074, China. E-mail: xiejia@hust.edu.cn

[b]State Key Laboratory of Materials Processing and Die & Mould Technology, School of Materials Science and Engineering, Huazhong University of Science and Technology, Wuhan 430074, China

† Electronic supplementary information (ESI) available. See DOI: 10.1039/d0ra07029g

doped activated carbon or nano-composites composed of metal oxides and N-doped carbon (NC).[46–48] N-doping can effectively enhance electronic conductivity and contributes extra pseudo-capacitive capacity, thus improving electrochemical performance.[49] Although CS is favored in constructing metal oxides/NC composites, so far, the preparation of SiO_x/NC composite anode materials by CS has not been reported.

In this work, for the first time, chitosan was used as a carbon precursor to fabricate micron-sized spherical SiO_x/NC composites. The strong hydrogen bonding effect between chitosan molecules and the hydrolyzed organosilica nanoparticles facilitates the uniform dispersion of the organosilica nanoparticles, consuming much less solvents than traditional Stöber method and finally ensuring the homogeneous distribution of SiO_x and NC. SiO_x/NC microspheres with average diameters less than 3 μm and controllable carbon content were synthesized with a scalable microemulsion method followed by carbonization. The uniform distribution of SiO_x nano-domains in NC can effectively enhance the structural integrity of SiO_x, leading to excellent long-term cycling performance. Due to the unique structural features and N-doping, the SiO_x/NC composite exhibited considerable capacitive-controlled Li storage capacity, which contributes to superior rate capability. Such electrochemical performances enabled stable full-cell operations when coupled with $LiFePO_4$. Consequently, after 350 cycles at 2C, the assembled SiO_x/NC-2//$LiFePO_4$ full cell maintains a capacity retention of 89%.

Experimental section

Sample preparation

To prepare the SiO_x/NC microspheres, 1 g of chitosan (CS, 200–400 mPa s, deacetylation degree ≥80%, Aladdin Chemistry Co.) and certain amounts of vinyltriethoxysilane (VTES, Aladdin Chemistry Co.) were used as the precursors of NC and SiO_x, respectively. The organosilica/chitosan (organosilica/CS) composites synthesized by adding 2, 2.5 and 3 g of VTES were designated as organosilica/CS-1, organosilica/CS-2, and organosilica/CS-3, respectively, and the corresponding carbonization products were labelled as SiO_x/NC-1, SiO_x/NC-2, and SiO_x/NC-3, respectively.

To synthesize SiO_x/NC-2, 1 g of chitosan was dispersed in 25 ml 1.5% acetic solution to form a transparent solution. After slowly adding 2.5 g of VTES, the solution was continuously stirred overnight at room temperature to obtain viscous organosilica/CS-2 solution. A well-mixed suspension containing 120 ml of liquid paraffin and 5.5 g of sorbitan trioleate (Span 85) was dispersed in a reactor and stirred at 1000 rpm for 0.5 h. Then the organosilica/CS-2 solution was added into the reactor and stirred at 1400 rpm for 1 h. Then, 3 g polyoxyethylene sorbitan trioleate (Tween 85) was added into the suspension and kept stirring at 1400 rpm for another 1 h. Subsequently, a solution containing 3 ml ammonia (28%) in 10 ml isopropanol was added dropwise into the vessel and stirred at 1400 rpm for 1 h to coagulate the organosilica/CS droplets. After vacuum filtration and washing with petroleum ether, ethanol, and deionized water (DW), the sample was dried in a freeze-dryer at −60 °C for 24 h. To obtain the black SiO_x/NC-2 powder, the freeze-dried white organosilica/CS-2 powders were carbonized at 1000 °C in a tube furnace for 3 h, in Ar/H_2 (95/5) atmosphere.

The synthesis of SiO_x/NC-1 and SiO_x/NC-3 were similar to that of SiO_x/NC-2, except the weight of VTES was 2 g and 3 g, respectively. Bare NC sample was prepared by etching SiO_x/NC-2 microspheres with 10% HF solution for 6 h.

Materials characterization

The Brunauer–Emmett–Teller (BET) specific surface area measurements of the SiO_x/NC composites were performed on a Micromeritics ASAP 2020 analyzer. To investigate the phase composition of the SiO_x/NC composites, a PANalytical X'Pert X-ray diffractometer was used to measure the X-ray diffraction (XRD) patterns. Thermo gravimetric analysis (TGA) data were collected by a STA-449C thermogravimetric apparatus in air atmosphere. X-ray photoelectron spectrum (XPS) data of the samples were obtained on a VG Multi Lab 2000 apparatus. Transmission-electron-microscopy (TEM) and scanning electron microscopy (SEM) images of the SiO_x/NC samples were taken by using a Tenia G200 FEI STEM/EDS microscope and a Nova NanoSEM 450 scanning electron microscope, respectively.

Measurements of electrochemical performances

The electrochemical performances of the SiO_x/NC composites and NC were tested by using CR2032 coin cells. The SiO_x/NC composite or bare NC, Super-P, and sodium alginate (75 : 10 : 15, by weight) were mixed in DW to form a slurry. Then the formed slurry was casted to a Cu foil. The mass loading of the active material was controlled at 0.9–1.2 mg cm^{-2}. The foil was dried at 100 °C in a vacuum oven over night. The electrolyte was 1.3 M lithium hexafluorophosphate ($LiPF_6$) in a mixed solution of ethylene carbonate/diethylene carbonate/fluoroethylene carbonate (EC/DEC/FEC, 30 : 60 : 10, by volume). The rate capability and cycling performance of the assembled half and full cells were tested galvanostatically on a Neware battery testing system. Cyclic voltammetry (CV) at various sweep rates was tested by using a Solartron 1470E electrochemical workstation. Electrochemical impedance spectroscopy (EIS) of the SiO_x/NC composites was tested by using a CHI600E electrochemical workstation. The N/P ratio of the SiO_x/NC-2//$LiPFeO_4$ (LFP) full cells was about 1.2. The weight ratio of LFP : Super-P : PVDF in the cathode was 80 : 10 : 10. The SiO_x/NC-2 anodes were pre-lithiated in half cells to contemplate the lithium loss of the initial lithiation process. The galvanostatical charge/discharge test of SiO_x/NC-2//LFP full cells were performed at 0.2–4C in a voltage range of 2.2–3.8 V. The capacities of the full cells are calculated based on the weight of LFP (1C = 170 mA h g^{-1}).

Results and discussion

The micron-sized SiO_x/NC microspheres were fabricated by a simple and scalable microemulsion method followed by high-

temperature carbonization, as illustrated in Fig. 1a. The microemulsion used in this work can be classified as water-in-oil (W/O) system. Before emulsification, VTES was slowly hydrolyzed and condensed in an acetic acid solution of CS to form organosilica nanoparticles. As shown in Fig. S1,† compared with raw CS, the obvious redshift of the vibration peaks of $-NH_2$ and –OH in organosilica/CS composite demonstrates the strong hydrogen binding effect between CS and the formed organosilica nanoparticles. In addition, with the hydrolysis and condensation of VTES, the CS solution gradually becomes more and more viscous, further confirming the strong hydrogen binding effect. Such strong hydrogen binding effect is beneficial for the uniform dispersion of the organosilica nanoparticles in the water phase. The water phase droplets were coagulated when ammonia was dropped into the emulsion system. After freeze-drying, the white organosilica/CS powder with homogeneous distribution of the organosilica nanoparticles in the CS matrix was obtained. The SiO_x/NC microspheres can be readily fabricated by pyrolysis of the organosilica/CS powder in Ar/H_2 atmosphere.

It is noteworthy that most of the SiO_x and nano-Si anode materials prepared by Stöber method consume extensive solvent (Table S1†). Consequently, the reported materials cannot be produced in a large scale. As shown in Table S1,† the solvent consumption in the hydrolysis process in this work is greatly reduced compared with the literature, which enables the large-scale synthesis of the SiO_x/NC composites. It is believed that the organosilica/CS solution can also be applied in the spray-drying method, which will facilitate more efficient preparation of micron-sized SiO_x/NC spheres.

The organosilica/CS samples are interconnected microspheres with smooth surface and compact structure (Fig. 1b, S2a and S3a†). As the organosilica content increases, the average diameter of the microspheres increases. After calcination, the SiO_x/NC samples inherited the smooth spherical morphology and compact structure of the organosilica/CS spheres (Fig. 1b, c, S2b and S3b†). According to the SEM and TEM observation, the average diameter of the SiO_x/NC microspheres also increases slightly with the increase of SiO_x content. According to the SEM and TEM (Fig. 1d) observation, the average particle sizes of SiO_x/NC-1, SiO_x/NC-2, and SiO_x/NC-3 are estimated to be ~0.8, 1.5, and 2.5 μm, respectively. Compared with nanomaterials, such micron-sized SiO_x/NC composites possess lower specific surface and higher tap

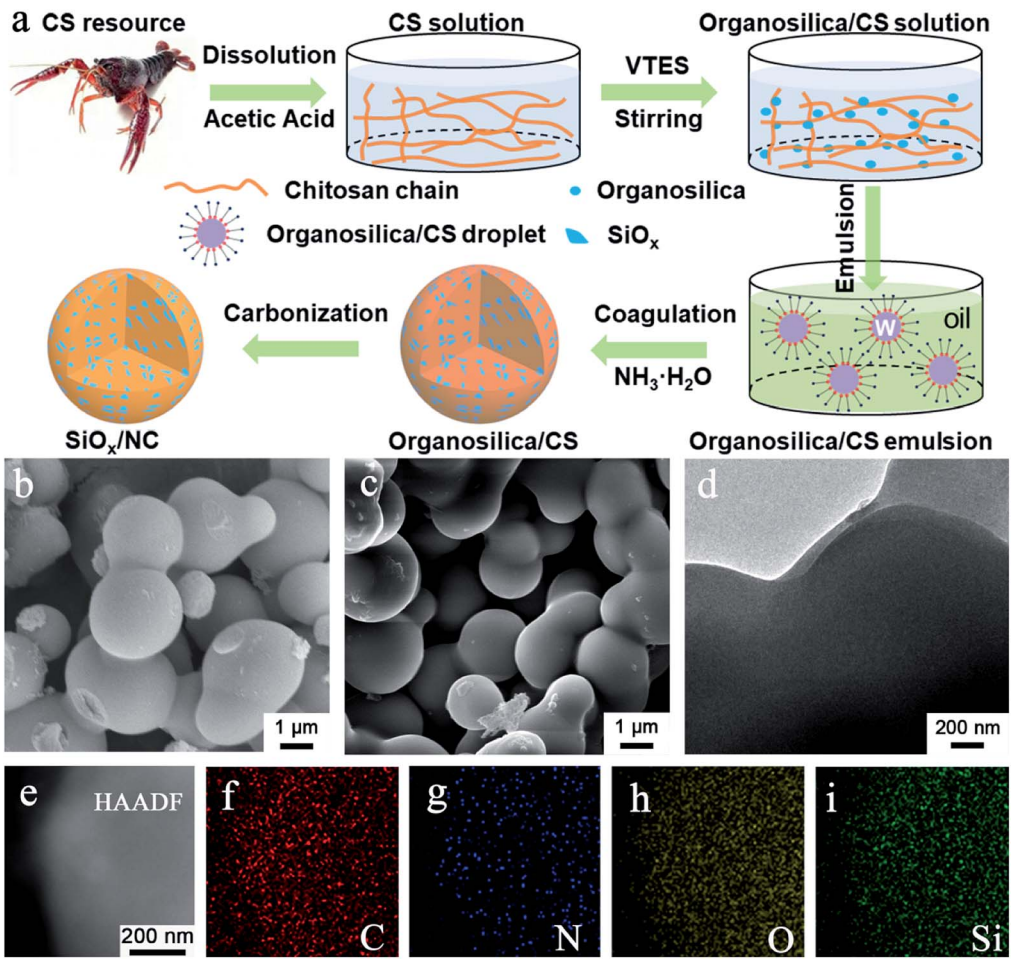

Fig. 1 (a) Fabrication process of SiO_x/NC microspheres, (b) SEM image of organosilica/CS-2, (c) SEM image of SiO_x/NC-2, (d) TEM and (e) HAADF-STEM images of SiO_x/NC-2, (f–i) EDS elemental mapping images corresponding to (e).

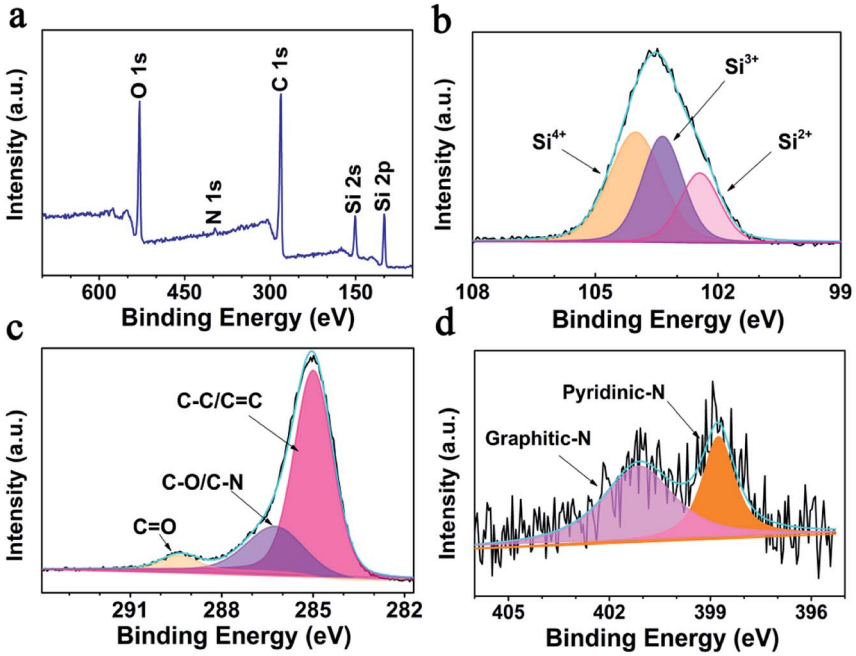

Fig. 2 XPS analysis of SiO_x/NC-2 (a) survey spectrum, (b–d) Si 2p, N 1s, and C 1s high-resolution spectra, respectively.

density, which is favorable for less side reaction and higher volumetric capacity.[50] The elemental mapping results (Fig. 1e–i) demonstrate that C, N, O, and Si distribute evenly in micron-sized SiO_x/NC spheres, indicating that the SiO_x nano-domains are also uniformly dispersed in NC matrix. The XRD patterns (Fig. S4†) of the SiO_x/NC composites are almost identical. Only some broad diffraction peaks can be identified, indicating that both the SiO_x and NC are amorphous. The broad diffraction peaks centered at ~23° and ~43° belong to SiO_x and NC, respectively. The Raman spectra of the SiO_x/NC composites are presented in Fig. S5.† The intense peaks located at approximately 1330 and 1600 cm^{-1} are corresponding to the D-band and G-band of NC, respectively. The I_D/I_G ratio for SiO_x/NC-1, SiO_x/NC-2, and SiO_x/NC-3 are estimated to be 1.12, 1.14, and 1.05, respectively, suggesting that a large number of defects have been introduced by N-doping. Two bumps of the 2D-band also appear at around 2650 and 2900 cm^{-1}, indicating the existence of graphitized carbon.[32]

The specific surface areas as well as pore size distribution of the SiO_x/NC composites are analyzed *via* nitrogen adsorption method (Fig. S6†). The obtained specific surface areas of the SiO_x/NC-1, SiO_x/NC-2, and SiO_x/NC-3 micron-sized spheres are 17.4, 10.5, and 6.0 $m^2\ g^{-1}$, respectively. The pore volumes of SiO_x/NC-1, SiO_x/NC-2, and SiO_x/NC-3 are 0.07, 0.04, and 0.03 $cm^3\ g^{-1}$, respectively. Such a micron-sized moderate porous spherical structure of SiO_x/NC is very favorable for obtaining high tap density, minimizing side effect as well as achieving high volumetric energy density. Thermogravimetric analysis (TGA) was performed in the air to estimate the SiO_x content of the SiO_x/NC composites. Based on the TGA results (Fig. S7†), the SiO_x contents of SiO_x/NC-1, SiO_x/NC-2, and SiO_x/NC-3 are calculated to be about 65%, 59%, and 51%, respectively. The actual SiO_x content of the SiO_x/NC composites should be slightly lower than the calculated results, because SiO_x domains are oxidized to SiO_2 during TGA testing.

Consistent with the EDS results, the XPS survey spectrum (Fig. 2a) reveals that the SiO_x/NC-2 sample is composed of Si, O, C, and N. After calcination at 1000 °C, the N 1s signal is very weak, and the N content of NC is determined to be 0.76 wt% by XPS elemental analysis. As shown in Fig. 2b, the broad high-resolution Si 2p peak are divided into three peaks, corresponding to Si^{2+}, Si^{3+}, and Si^{4+} respectively. The Si^{2+} : Si^{3+} : Si^{24+} ratio is calculated to be 21.36% : 33.62% : 45.02%, and an average valence state of 3.24 is determined (corresponding to an x value of 1.62). The calculated average valence state value is very close to the theoretical one (3.0). The C 1s spectrum (Fig. 2c) can be divided into three peaks, locating at 284.9, 286.2, and 289.4 eV, corresponding to C–C/C=C, C–N/C–O, and C=O bonds, respectively.[51,52] Fig. 2d presents the high resolution N 1s spectrum. The peak located at 401.1 eV is attributed to graphitic-N, and the one centered at 398.9 eV corresponds to pyridinic-N.[25] It has been reported that N-doping is beneficial to improve the electron/ion conductivity of the carbon matrix.[53]

As shown in Fig. 3a and S8,† the initial CV curves of the SiO_x/NC electrodes scanned at 0.1 mV s^{-1} are similar in shape. In the first cathodic process, the peak at ~1.2 V corresponds to the formation of the solid electrolyte interface (SEI) layer.[19] The peak located at ~0.75 V cannot be observed in the following cycles. This peak relates to the irreversible reaction between Li and SiO_x, and the formation of Si, Li_2O, and various lithium silicates.[19] The sharp cathodic peak close to 0.01 V is ascribed to lithiation of the *in situ* formed Si. The broad anodic peak below 1.2 V is associated with the delithiation of Li_xSi alloy and the formation of amorphous Si.[19] A reduction peak at ~0.22 V

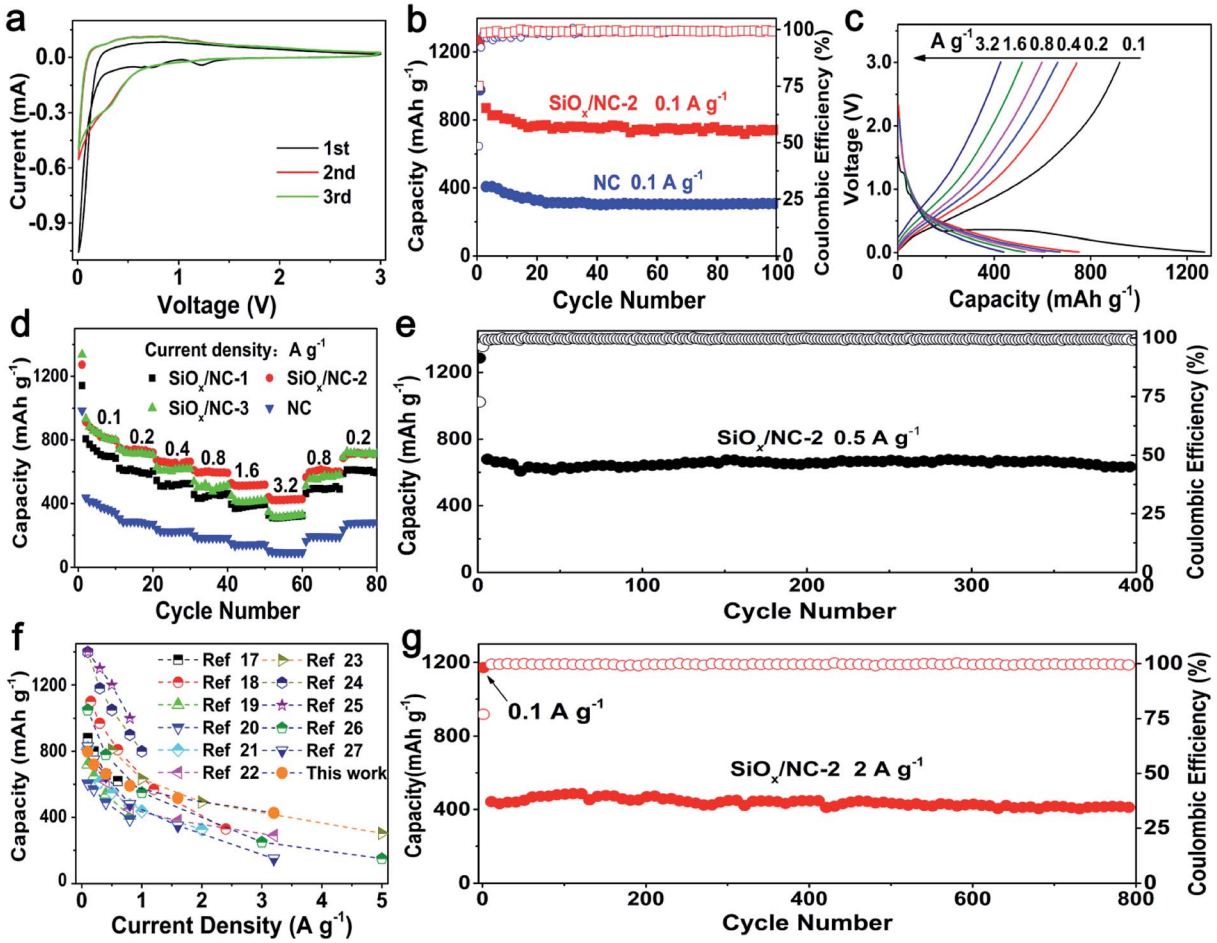

Fig. 3 (a) CV curves of SiO_x/NC-2, (b) cycling performance of SiO_x/NC-2 and NC at 0.1 A g^{-1}, (c) galvanostatic charge–discharge curves of SiO_x/NC-2 and NC at 0.1–3.2 A g^{-1}, (d) rate performance of the NC and SiO_x/NC electrodes, (e) cycling performance of SiO_x/NC-2 at 0.5 A g^{-1}, (f) comparison of the rate performance of SiO_x/NC-2 and literature, (g) long-term cycling performance of SiO_x/NC-2 at 2 A g^{-1}.

appeared in the subsequent cycles, corresponding to the lithiation of the amorphous Si. The perfect overlap of the second and third curves indicates that the lithiation/delithiation reaction is highly reversible.

The cycling performance of SiO_x/NC-2 and bare NC at 0.1 A g^{-1} are shown in Fig. 3b. SiO_x/NC-2 maintains a discharge capacity of 742 mA h g^{-1} after 100 cycles, corresponding to a capacity retention of 81.1% to the 2nd capacity. On the contrast, the bare NC electrode only maintains a specific capacity of 307 mA h g^{-1}, demonstrating that SiO_x contributes most of the capacity of the SiO_x/NC composites. The selected charge–discharge profiles of SiO_x/NC-2 at 0.1 A g^{-1} are presented in Fig. S10.† SiO_x/NC-2 manifests an initial discharge capacity of 1270 mA h g^{-1} as well as an initial coulombic efficiency (ICE) of 74.9%. Such ICE is higher than many recently reported SiO_x anodes.[17,19,20,22,23,28]

Fig. 3c displays the typical charge–discharge curves of SiO_x/NC-2 at 0.1–3.2 A g^{-1} and Fig. 3d reveals the rate capability of bare NC and the SiO_x/NC electrodes. The corresponding discharge specific capacity data are listed in Table S2.† These samples exhibit a stable cycling even at 3.2 A g^{-1}. The electrodes can recover nearly 100% of the initial capacities, when the current density decreases to 0.2 A g^{-1}, demonstrating the structural integrity of bare NC and the SiO_x/NC microspheres. The capacity difference between SiO_x/NC-2 and SiO_x/NC-3 is negligible at 0.1 and 0.2 A g^{-1}. While at 0.8, 1.6, and 3.2 A g^{-1}, SiO_x/NC-2 achieves discharge capacities of 592, 518, and 427 mA h g^{-1}, respectively, evidently higher than the corresponding ones of SiO_x/NC-3, although SiO_x/NC-3 has a higher content of SiO_x. The lower capacities of SiO_x/NC-3 at high current densities can be explained by its higher charge-transfer resistance, which can be confirmed by the EIS spectra (Fig. S9†). At 0.2 and 3.2 A g^{-1}, the bare NC electrode only delivers a capacity of 271 and 92 mA h g^{-1}, respectively, confirming that SiO_x is the primary active material. Fig. 3f compares the rate performance of SiO_x/NC-2 and many reported SiO_x/C composites with x values close to 1.5.[17–27] For some reported SiO_x/C composites, the rate performance are tested at current densities lower than 2 A g^{-1}, and their capacities decrease sharply with the increase of current density. Some SiO_x/C composites deliver much higher capacities than SiO_x/NC-2 at 0.1 and 0.2 A g^{-1}, but at about 3.2 A g^{-1}, their discharge capacities are lower than that of SiO_x/NC-2. At 3.2 A g^{-1}, SiO_x/NC-2 exhibits a discharge capacity of 427 mA h g^{-1}, which is quite competitive among the

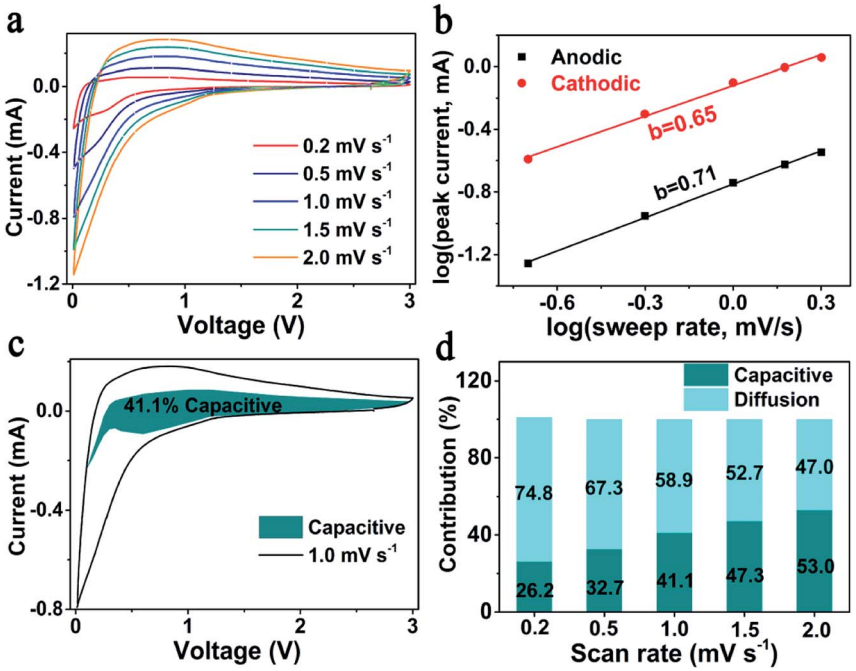

Fig. 4 (a) CV curves of SiO_x/NC-2 at 0.2–2.0 mV s^{-1}, (b) plots of log (i_p) *vs.* log (v), (c) capacitive-controlled contribution at 1 mV s^{-1}, (d) capacitive-controlled contribution at 0.2–2.0 mV s^{-1}.

recently reported SiO_x-based composite electrodes. The superior rate capability of SiO_x/NC-2 may be derived from the uniform dispersion of SiO_x as well as N-doping.[17,32,46]

As shown in Fig. 3e and g, the SiO_x/NC-2 also shows excellent long-term cycling performance at both 0.5 and 2 A g^{-1}. After 400 deep charge–discharge cycling at 0.5 A g^{-1}, SiO_x/NC-2 maintains a discharge capacity of 637 mA h g^{-1}, slightly lower than the capacity of the SiO_x/C microspheres prepared with resorcinol/formaldehyde and VTES by Liu *et al.*[17] However, the SiO_x/NC-2 displays outstanding long-term cycling capability at a high current density of 2 A g^{-1}, and retains a discharge capacity of 416 mA h g^{-1} after 800 cycles, corresponding to a capacity retention of 81% from the 4th cycle. The excellent cycling stability of SiO_x/NC-2 benefits from its outstanding structural integrity. As shown in Fig. S11,† after 100 cycles, the SiO_x/NC-2 preserves the micron-sized spherical geometry, demonstrating

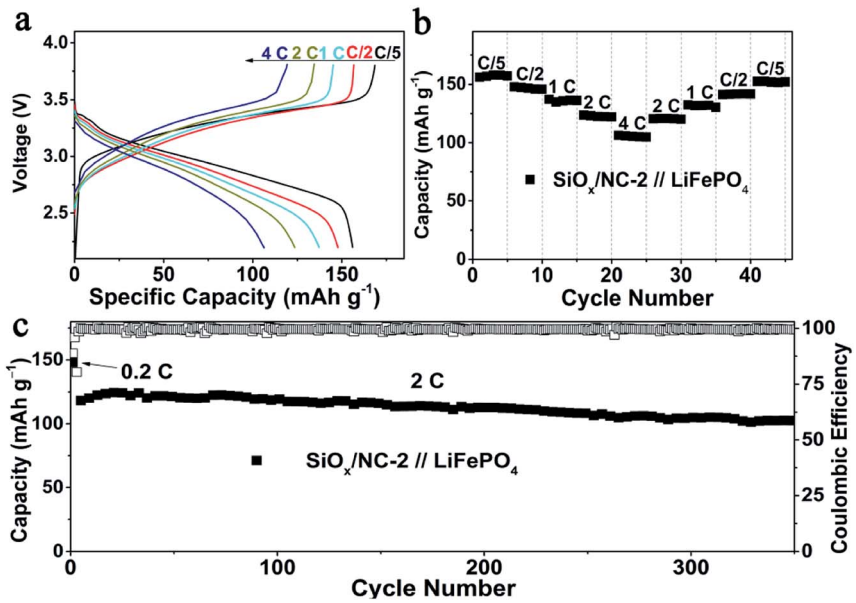

Fig. 5 Electrochemical performance of the SiO_x/NC-2//LFP full cell, (a) galvanostatic charge/discharge profiles at 0.2–4C, (b) rate capability at 0.2–4C, (c) galvanostatic long cycling performance at 2C.

its structural integrity. The structural integrity originates from the unique structural features of SiO_x/NC-2: (a) the SiO_x species are divided into ultrafine nano-domains by the 3D NC matrix, thus the pulverization of SiO_x can be effectively inhibited. (b) The NC matrix ensures the structural integrity of the micron-sized composite spheres by buffering the volume change of the SiO_x nano-domains and preventing their aggregation.

According to previous reports, the outstanding rate performance may be related with the capacitive-controlled Li storage mechanism.[54,55] Here, CV measurements at sweep rates of 0.2–2.0 mV s^{-1} were performed, to explore the Li storage mechanism of SiO_x/NC-2. The obtained CV curves showed similar shapes with broad peaks (Fig. 4a). Generally, the capacitive behavior can be judged based on eqn (1).[54]

$$i_p = av^b \quad (1)$$

Here, i_p and v correspond to peak current and sweep rate, respectively. a is a constant, and b is the slope of the log (v) − log (i_p) plots. It is commonly accepted that a b-value of 0.5 and 1 indicates a diffusion-controlled and a capacitive-controlled Li storage mechanism, respectively. As displayed in Fig. 4b, the determined b-value of the anodic peak is 0.71, and the one of the cathodic peak is 0.65. These b-values suggest that both the capacitive-controlled and diffusion-controlled Li storage mechanisms contribute to the SiO_x/NC-2 electrode. At a specific scan rate (v) and voltage (V), based on the relationship between current ($i_{(V)}$), capacitive-controlled contribution (k_1v), and diffusion-controlled contribution ($k_2v^{1/2}$): $i(V) = k_1v + k_2v^{1/2}$, the ratio of capacitive-controlled capacity to the total Li storage capacity can be calculated quantitatively.[54,55] Typically, at 1 mV s^{-1} (Fig. 4c), capacitive-controlled capacity accounts for about 41.1% of the total Li storage capacity. The ratio of capacitive-controlled capacity to the total capacity increases with the sweep rate (Fig. 4d), demonstrating that the capacitive-controlled mechanism facilitates more efficient Li^+ insertion/extraction at higher scan rate. As a result, the SiO_x/NC-2 electrode exhibits high rate capability and stable cycling at 2 A g^{-1}. The pseudocapacitive effect of SiO_x/NC-2 can be attributed to three factors: (a) the huge interfaces between SiO_x nano-domains and NC matrix provide numerous active sites for Li storage; (b) N doping causes sufficient defects in the carbon matrix, thus enhances electron/ion transfer kinetics; (c) the uniform distribution of SiO_x in NC matrix reduces the diffusion distance of electron and Li^+, leading to further improved electrochemical kinetics.

To evaluate the validity of the SiO_x/NC-2 in LIBs, SiO_x/NC-2//LFP full cells were assembled by using commercial LFP and SiO_x/NC-2 as a cathode and anode, respectively. The N/P ratio of the full cell is controlled at around 1.2. Before the full cell assembly, the SiO_x/NC-2 electrodes were pre-lithiated in a half cell to obtain a stable SEI layer. Base on the weight of LFP, at 0.2, 0.5, 1, 2 and 4C, the SiO_x/NC-2//LFP full cell manifests specific capacities of 156, 148, 137, 123 and 106 mA h g^{-1}, respectively (Fig. 5a). Due to the excellent rate capability of SiO_x/NC-2, the assembled SiO_x/NC-2//LFP full cell displays stable cycling at 4C (Fig. 5b). A specific capacity of 152 mA h g^{-1} is achieved, when the C-rate gradually decreases to 0.2C, demonstrating superior rate capability. The superior rate capability of the SiO_x/NC-2//LFP full cell can be attributed to the enhanced structural integrity and the dual-model (battery-capacitive) Li storage mechanism of SiO_x/NC-2. Consequently, the as assembled SiO_x/NC-2//LFP full cell achieves a stable long-term cycling at a relatively high rate of 2C (Fig. 5c). After 350 cycles, the SiO_x/NC-2//LFP full cell maintains a specific capacity of 103 mA h g^{-1}, retaining 89% of the 3rd capacity. The superior rate capability and outstanding cycling stability demonstrate that the SiO_x/NC-2//LFP full cell can serve as a potential high energy density power source with a certain quick-charge capability.

The superior rate capability and excellent cycling stability of SiO_x/NC-2 can be ascribed to the following points: (a) the electron and Li^+ diffusion kinetics of active SiO_x is significantly enhanced by its even distribution in the NC matrix. (b) The NC matrix ensures the structural integrity by alleviating the volume change and preventing the pulverization of SiO_x. (c) The capacitive-controlled Li storage mechanism enables the high rate capability.

Conclusions

In summary, micron-sized SiO_x/NC interconnected microspheres with tunable SiO_x content (51–65 wt%) have been produced *via* a scalable microemulsion method with chitosan and VETS as the NC and SiO_x precursor, respectively. With the uniform distribution of ultra-small SiO_x domains in amorphous NC matrix, the SiO_x/NC-2 microspheres exhibit considerable capacitive-controlled Li storage capacity and outstanding structural integrity, which contribute to the superior rate capability and excellent cycling stability. After 350 cycles at 2C, the assembled SiO_x/NC-2//LFP full cell can maintain a specific capacity of 103 mA h g^{-1}. This work provides an effective approach for constructing micron-sized high-performance SiO_x/C anode materials by using chitosan as N-doped carbon precursor, and to some extent facilitates the recycling of waste seafood shells.

Conflicts of interest

There are no conflicts to declare.

Acknowledgements

This work was supported by the National Natural Science Foundation of China (No. 51821005, 21975087, U1966214, 51902116). We gratefully acknowledge the Analytical and Testing Center of HUST for allowing us to use its facilities.

References

1 M. N. Obrovac and V. L. Chevrier, *Chem. Rev.*, 2014, **114**, 11444–11502.
2 Y.-M. Chiang, *Science*, 2010, **330**, 1485.
3 S. Choi, T. W. Kwon, A. Coskun and J. W. Choi, *Science*, 2017, **357**, 279–283.

4 J. B. Goodenough and K. S. Park, *J. Am. Chem. Soc.*, 2013, **135**, 1167–1176.
5 Y. Sun, N. Liu and Y. Cui, *Nat. Energy*, 2016, **1**, 16071.
6 X. Zuo, J. Zhu, P. Müller-Buschbaum and Y. J. Cheng, *Nano Energy*, 2017, **31**, 113–143.
7 J. Yang, Y. Wang, W. Li, L. Wang, Y. Fan, W. Jiang, W. Luo, Y. Wang, B. Kong, C. Selomulya, H. K. Liu, S. X. Dou and D. Zhao, *Adv. Mater.*, 2017, **29**, 1700523.
8 H. Shang, Z. Zuo, L. Yu, F. Wang, F. He and Y. Li, *Adv. Mater.*, 2018, **30**, 1801459.
9 X. Hui, R. Zhao, P. Zhang, C. Li, C. Wang and L. Yin, *Adv. Energy Mater.*, 2019, **9**, 1901065.
10 J. Sung, J. Ma, S.-H. Choi, J. Hong, N. Kim, S. Chae, Y. Son, S. Y. Kim and J. Cho, *Adv. Mater.*, 2019, **31**, 1900970.
11 L. Zhang, J. Deng, L. Liu, W. Si, S. Oswald, L. Xi, M. Kundu, G. Ma, T. Gemming, S. Baunack, F. Ding, C. Yan and O. G. Schmidt, *Adv. Mater.*, 2014, **26**, 4527–4532.
12 Z. Li, H. Zhao, P. Lv, Z. Zhang, Y. Zhang, Z. Du, Y. Teng, L. Zhao and Z. Zhu, *Adv. Funct. Mater.*, 2018, **28**, 1605711.
13 Z. Liu, Q. Yu, Y. Zhao, R. He, M. Xu, S. Feng, S. Li, L. Zhou and L. Mai, *Chem. Soc. Rev.*, 2019, **48**, 285–309.
14 J. Lee, J. Moon, S. A. Han, J. Kim, V. Malgras, Y.-U. Heo, H. Kim, S.-M. Lee, H. K. Liu, S. X. Dou, Y. Yamauchi, M.-S. Park and J. H. Kim, *ACS Nano*, 2019, **13**, 9607–9619.
15 Q. Xu, J.-K. Sun, Y.-X. Yin and Y.-G. Guo, *Adv. Funct. Mater.*, 2018, **28**, 1705235.
16 J. Wang, H. Zhao, J. He, C. Wang and J. Wang, *J. Power Sources*, 2011, **196**, 4811–4815.
17 Z. Liu, D. Guan, Q. Yu, L. Xu, Z. Zhuang, T. Zhu, D. Zhao, L. Zhou and L. Mai, *Energy Storage Mater.*, 2018, **13**, 112–118.
18 J. Han, G. Chen, T. Yan, H. Liu, L. Shi, Z. An, J. Zhang and D. Zhang, *Chem. Eng. J.*, 2018, **347**, 273–279.
19 Y. Ren and M. Li, *J. Power Sources*, 2016, **306**, 459–466.
20 Y. Ren, X. Wu and M. Li, *Electrochim. Acta*, 2016, **206**, 328–336.
21 C. H. Gao, H. L. Zhao, J. Wang, J. Wang, C. L. Yan and H. Q. Yin, *J. Electrochem. Soc.*, 2019, **166**, A574–A581.
22 Z. Sang, Z. Zhao, D. Su, P. Miao, F. Zhang, H. Ji and X. Yan, *J. Mater. Chem. A*, 2018, **6**, 9064–9073.
23 M. Han and J. Yu, *J. Power Sources*, 2019, **414**, 435–443.
24 J. Zhang, X. Zhang, C. Zhang, Z. Liu, J. Zheng, Y. Zuo, C. Xue, C. Li and B. Cheng, *Energy Fuels*, 2017, **31**, 8758–8763.
25 J. Zhang, C. Zhang, Z. Liu, J. Zheng, Y. Zuo, C. Xue, C. Li and B. Cheng, *J. Power Sources*, 2017, **339**, 86–92.
26 L. Sun, T. Su, L. Xu, M. Liu and H.-B. Du, *Chem. Commun.*, 2016, **52**, 4341–4344.
27 H. Ming, J. Qiu, S. Zhang, M. Li, X. Zhu, L. Wang and J. Ming, *ChemElectroChem*, 2017, **4**, 1165–1171.
28 J. Hu, L. Fu, R. Rajagopalan, Q. Zhang, J. Luan, H. Zhang, Y. Tang, Z. Peng and H. Wang, *ACS Appl. Mater. Interfaces*, 2019, **11**, 27658–27666.
29 C. Guo, D. Wang, T. Liu, J. Zhu and X. Lang, *J. Mater. Chem. A*, 2014, **2**, 3521–3527.
30 Z. Liu, Y. Zhao, R. He, W. Luo, J. Meng, Q. Yu, D. Zhao, L. Zhou and L. Mai, *Energy Storage Mater.*, 2019, **19**, 299–305.
31 Q. Xu, J.-K. Sun, Z.-L. Yu, Y.-X. Yin, S. Xin, S.-H. Yu and Y.-G. Guo, *Adv. Mater.*, 2018, **30**, 1707430.
32 G. Zhu, F. Zhang, X. Li, W. Luo, L. Li, H. Zhang, L. Wang, Y. Wang, W. Jiang, H. K. Liu, S. X. Dou and J. Yang, *Angew. Chem., Int. Ed.*, 2019, **58**, 6669–6673.
33 Y. Chen, Q. Mao, L. Bao, T. Yang, X. Lu, N. Du, Y. Zhang and Z. Ji, *Ceram. Int.*, 2018, **44**, 16660–16667.
34 D. Liu, C. Chen, Y. Hu, J. Wu, D. Zheng, Z.-z. Xie, G. Wang, D. Qu, J. Li and D. Qu, *Electrochim. Acta*, 2018, **273**, 26–33.
35 P. S. Bakshi, D. Selvakumar, K. Kadirvelu and N. S. Kumar, *Int. J. Biol. Macromol.*, 2020, **150**, 1072–1083.
36 X. Chen, H. Yang and N. Yan, *Chem.–Eur. J.*, 2016, **22**, 13402–13421.
37 Y. Ning and C. Xi, *Nature*, 2015, **524**, 155.
38 L. Gao, J. Ma, S. Li, D. Liu, D. Xu, J. Cai, L. Chen, J. Xie and L. Zhang, *Nanoscale*, 2019, **11**, 12626–12636.
39 J. Ma, L. Gao, S. Li, Z. Zeng, L. Zhang and J. Xie, *Batteries Supercaps*, 2020, **3**, 165–173.
40 C. Chen, S. H. Lee, M. Cho, J. Kim and Y. Lee, *ACS Appl. Mater. Interfaces*, 2016, **8**, 2658–2665.
41 Y. Gao, X. Qiu, X. Wang, A. Gu, L. Zhang, X. Chen, J. Li and Z. Yu, *ACS Sustainable Chem. Eng.*, 2019, **7**, 16274–16283.
42 X. Zhao, C.-H. Yim, N. Du and Y. Abu-Lebdeh, *J. Electrochem. Soc.*, 2018, **165**, A1110–A1121.
43 J. Y. Han, Y. Huang, Y. Chen, A. M. Song, X. H. Deng, B. Liu, X. Li and M. S. Wang, *ChemElectroChem*, 2020, **7**, 1213–1224.
44 M. Ogino, D. Kotatha, Y. Torii, K. Shinomiya, S. Uchida, T. Furuike, H. Tamura and M. Ishikawa, *Electrochemistry*, 2020, **88**, 132–138.
45 H. Z. Yang, Y. Liu, L. B. Kong, L. Kang and F. Ran, *J. Power Sources*, 2019, **426**, 47–54.
46 C. Han, L. Xu, H. Li, R. Shi, T. Zhang, J. Li, C.-P. Wong, F. Kang, Z. Lin and B. Li, *Carbon*, 2018, **140**, 296–305.
47 S. Huang, Z. Li, B. Wang, J. Zhang, Z. Peng, R. Qi, J. Wang and Y. Zhao, *Adv. Funct. Mater.*, 2018, **28**, 1706294.
48 C. Li, X. Zhang, K. Wang, X. Sun and Y. Ma, *Carbon*, 2018, **140**, 237–248.
49 Q. Niu, K. Gao, Q. Tang, L. Wang, L. Han, H. Fang, Y. Zhang, S. Wang and L. Wang, *Carbon*, 2017, **123**, 290–298.
50 H. Jia, J. Zheng, J. Song, L. Luo, R. Yi, L. Estevez, W. Zhao, R. Patel, X. Li and J.-G. Zhang, *Nano Energy*, 2018, **50**, 589–597.
51 S.-Z. Zeng, Y. Niu, J. Zou, X. Zeng, H. Zhu, J. Huang, L. Wang, L. B. Kong and P. Han, *J. Power Sources*, 2020, **466**, 228234.
52 Y. Zhang, G. Hu, Q. Yu, Z. Liu, C. Yu, L. Wu, L. Zhou and L. Mai, *Mater. Chem. Front.*, 2020, **4**, 1656–1663.
53 W. Luo, F. Li, J.-J. Gaumet, P. Magri, S. Diliberto, L. Zhou and L. Mai, *Adv. Energy Mater.*, 2018, **8**, 1703237.
54 R. Xu, G. Wang, T. Zhou, Q. Zhang, H. P. Cong, S. Xin, J. Rao, C. Zhang, Y. Liu and Z. Guo, *Nano Energy*, 2017, **39**, 253–261.
55 T. Brezesinski, J. Wang, S. H. Tolbert and B. Dunn, *Nat. Mater.*, 2010, **9**, 146–151.